Anisotropic Second- and Third-Harmonic Hermite–Gaussian Beam Generation with NbOI$_2$ Holograms

Jayanta Deka, Jie Gao,* and Xiaodong Yang*

Hermite–Gaussian (HG) modes are an orthogonal set of solutions to the paraxial wave equation possessing distinct spatial intensity variations, which are important in many optical applications. Here, anisotropic second- and third-harmonic HG beam generation is demonstrated with ultrathin niobium oxide diiodide (NbOI$_2$) grating holograms to produce the nonlinear HG$_{01}$ and HG$_{10}$ modes. It is shown that the generated second-harmonic HG modes exhibit a high anisotropy ratio reaching a large value of 14.95, while the simultaneously generated third-harmonic HG modes have an anisotropy ratio up to 4.85. The relative magnitudes of the second- and third-order nonlinear susceptibility tensor elements of NbOI$_2$ crystal are extracted by analyzing the polarization-dependent nonlinear emission. These demonstrations provide new opportunities for building functional polarization-sensitive nonlinear optical devices used for future integrated photonic chips, optical computing, and optical communication.

1. Introduction

Hermite–Gaussian (HG) and Laguerre–Gaussian (LG) modes are different families of complete sets of orthogonal spatial modes, which are solutions to the paraxial wave equation.[1] The HG modes, also known as transverse modes, have linear phase fronts and can be described by two mode indices (m, n) which are separable in Cartesian coordinates, while the LG modes have spiral phase fronts possessing orbital angular momentum and can be described by the topological charge l. It is known that by shaping the optical wavefront of an optical beam, important beam parameters such as orbital angular momentum and spatial intensity variation can be controlled.

J. Deka, X. Yang
Department of Mechanical and Aerospace Engineering
Missouri University of Science and Technology
Rolla 65409, MO, USA
E-mail: yangxia@mst.edu

J. Gao
Department of Mechanical Engineering
Stony Brook University
Stony Brook 11794, NY, USA
E-mail: jie.gao.5@stonybrook.edu

The ORCID identification number(s) for the author(s) of this article can be found under https://doi.org/10.1002/adpr.202500188.

The generation and manipulation of HG beams and other higher-order optical modes with complex beam profiles have profound implications across various applications including precision lithography,[2] optical sensing,[3] optical trapping,[4,5] optical communication,[6–8] and gravitational wave detection.[9] Most of the existing optical beam wavefront shaping components such as phase plates and spatial light modulators are bulky and not readily compatible with on-chip integration. Recently, plasmonic metasurfaces with the ability to control the amplitude and phase of an impinging optical wavefront have been used for beam shaping.[10,11] The beam shaping techniques have been extended from the linear regime into the nonlinear regime to introduce new frequencies as an extra degree of freedom for light-matter interactions,[12] which enables many applications such as the entangled mode generation in quantum optics.[13] However, plasmonic metasurfaces often face challenges in nonlinear beam shaping due to inherent high optical loss, low damage threshold, and limited optical nonlinearity.

2D materials have garnered tremendous attention in optical technologies due to their exceptional linear and nonlinear optical properties. The remarkable optical properties, along with the reduced dimensionality of 2D materials, offer great potential for developing functional chip-scale optical devices.[14] In the nonlinear regime, various types of 2D materials and their heterostructures have been extensively studied for their tailorable optical responses in second-harmonic generation (SHG), third-harmonic generation (THG), sum-frequency generation, four-wave mixing, and saturable absorption.[15–18] The reduced dimensionality also makes 2D materials a suitable platform for making nonlinear optical devices without the requirement of complex phase-matching techniques. On the other hand, highly anisotropic optical properties due to low in-plane crystalline symmetry have been reported for different types of 2D materials such as black phosphorus (BP), GeS, GeSe, SiP, TiS$_3$, As$_2$S$_3$, ReS$_2$, SnS, and GeAs,[19–25] which have great potential for building various functional polarization-sensitive optical devices such as optical sensors,[26] lasers[27] and photodetectors.[28,29] In this context, niobium oxide dihalides (NbOX$_2$) are a new class of ferroelectric 2D materials exhibiting strong and anisotropic nonlinear optical responses. The existence of strong in-plane ferroelectricity of NbOX$_2$ presents significant potential for realizing energy storage devices.[30] The ferroelectric-to-paraelectric phase transition of NbOX$_2$ under external stimuli can induce significant changes in their linear and nonlinear optical properties,

which holds great promise for building optical sensing and switching devices.[31] Ferroelectricity is also associated with inherent broken inversion symmetry of $NbOX_2$ crystal, leading to strong SHG responses. It has been reported that $NbOX_2$ crystals exhibit much higher second-order nonlinear optical susceptibilities compared to other 2D materials and conventional nonlinear media.[32,33] Highly anisotropic and tunable SHG emission from these materials have also been reported, which has strong potential to build ultrathin polarization-sensitive optical devices.[33–35]

In this work, anisotropic second- and third-harmonic HG beams are generated simultaneously from ultrathin $NbOI_2$ grating holograms for producing the nonlinear HG_{01} and HG_{10} modes. The binary-amplitude holograms are utilized to encode the beam profile information of the HG_{01} and HG_{10} modes, and the generated HG beams are recorded in far-field diffraction images. It is demonstrated that the generated second-harmonic HG modes display a high anisotropy ratio, attaining a large value of 14.95, while the third-harmonic HG modes have an anisotropy ratio reaching up to 4.85. Furthermore, the relative magnitudes of the second- and third-order nonlinear susceptibility tensor elements of the $NbOI_2$ bare flakes and the fabricated holograms are retrieved by analyzing the polarization-dependent SHG and THG emission. These demonstrated results open up new avenues for building 2D material-based polarization-sensitive nonlinear optical devices with tailored functionalities used for future photonic integrated circuits, quantum photonic chips, optical computing, and optical communication.

2. Results and Discussion

The side view illustrations of the $NbOI_2$ lattice structure along the b-axis and c-axis are shown in **Figure 1**a. The $NbOI_2$ layers

are stacked together along the a-axis with weak van der Waals forces with the interlayer distance of 0.75 nm. The $NbOI_2$ lattice crystallizes in monoclinic structure belonging to C2 space group with unit cell dimensions of $a = 15.11$ Å, $b = 3.94$ Å, $c = 7.53$ Å and $\beta = 103.84°$ at room temperature.[31] The Nb atoms exhibit a 1D Peierls distortion, resulting in nonequal distances between two Nb atoms along the c-axis ($L_1 \neq L_2$) and the nonequal distances of an Nb atom from two neighboring O atoms along the b-axis ($D_1 \neq D_2$). The displacement of the Nb atoms gives rise to spontaneous polarization along the b-axis. The optical microscope image and the atomic force microscopy (AFM) image of an exfoliated $NbOI_2$ flake with the thickness of 80 nm on glass substrate are shown in Figure 1b,c. The SHG and THG emission from the flake is characterized with nonlinear optical spectroscopy and pump power-dependance measurements. The measured SHG and THG spectra are plotted in Figure 1d,f with the excitation wavelength at 1560 nm, showing the nonlinear emission peaks at 780 and 520 nm, which are exactly half and one-third of the excitation wavelength corresponding to the SHG and THG processes, respectively. Next, the nonlinear optical processes are further studied with the pump power dependance plotted in Figure 1e,g. The slopes of the curves from the log–log scale plots are estimated to be 1.98 and 2.98, which are consistent with the SHG and THG nonlinear optical processes, respectively.

Next, polarization-resolved SHG and THG measurements are performed on the 80 nm-thick flake shown in Figure 1 to determine the anisotropic nonlinear optical properties of $NbOI_2$ crystal. The optical setup for the polarization-resolved nonlinear measurements is illustrated in **Figure 2**. The pump polarization angle with respect to the c-axis of the crystal is determined by using a linear polarizer and a rotating half-wave plate placed in the excitation path. In the parallel or perpendicular
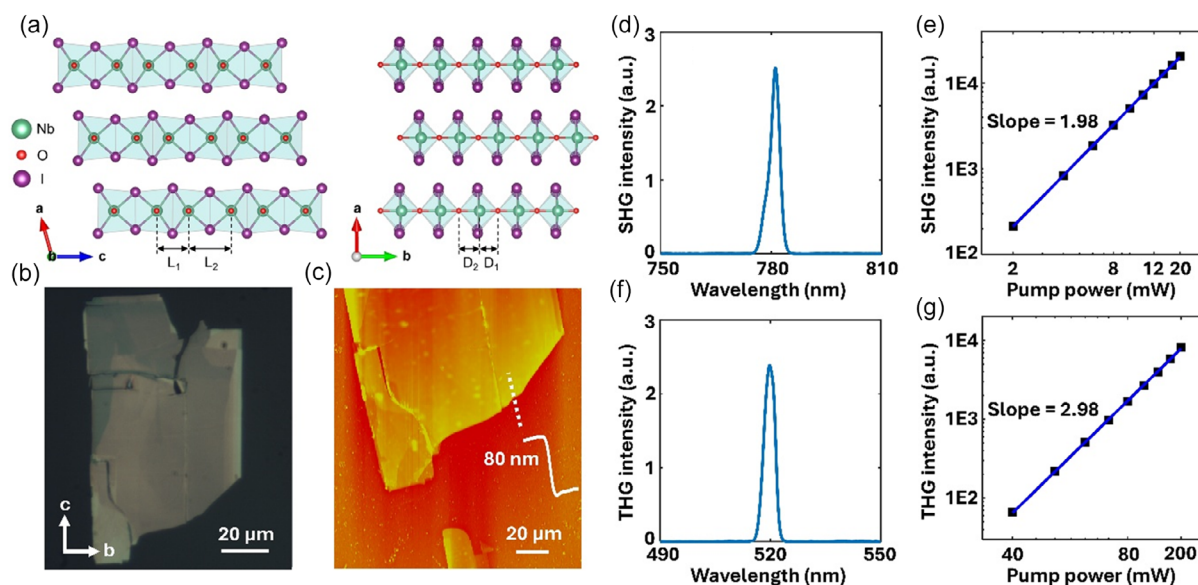

Figure 1. Characterization of SHG and THG responses of the $NbOI_2$ flake. a) Side view illustrations of the $NbOI_2$ lattice structure showing nonequal distances between two Nb atoms along the c-axis ($L_1 \neq L_2$) and nonequal distances of an Nb atom from two neighboring O atoms along the b-axis ($D_1 \neq D_2$). b) Optical microscope image and c) AFM image of a $NbOI_2$ flake on glass substrate. d) Measured SHG spectrum of the $NbOI_2$ flake. e) Pump power dependance of the SHG emission in log–log scale. f) Measured THG spectrum of the $NbOI_2$ flake. g) Pump power dependance of the THG emission in log–log scale.
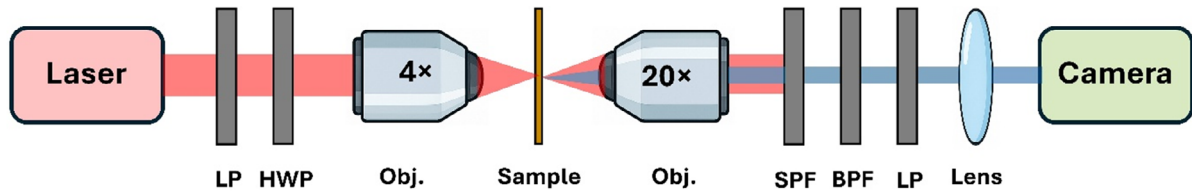
Figure 2. The optical setup for the polarization-resolved SHG and THG measurements. LP: linear polarizer, HWP: half-wave plate, Obj.: objective lens, SPF: shortpass filter, BPF: bandpass filter.

polarization configuration for the SHG measurements, the direction of the linear polarizer in the collection path is set to be parallel or perpendicular to the linear polarization direction of the pump beam. To measure the b-component or c-component of THG emission, the linear polarizer in the collection path is fixed along the direction of the b-axis or c-axis of the crystal. The parallel and perpendicular components of SHG emission and the total SHG intensity as a function of the pump polarization angle with respect to the c-axis are shown in **Figure 3**a–c at the excitation wavelength of 1560 nm. The parallel component of SHG emission shows a twofold profile with the maximum SHG intensity along the b-axis, while the perpendicular component of SHG emission has a butterfly-shaped profile oriented along the c-axis. It is found that the perpendicular component of SHG emission is significantly weaker than the parallel component, leading to a twofold profile along the b-axis for the total SHG intensity. The measured SHG anisotropy ratio, defined as the ratio between the maximum and minimum intensities, is 17.73 for the flake. For NbOI₂ crystal belonging to monoclinic C2 space group, the parallel and perpendicular components of SHG emission can be expressed as,[36]

$$I_{2\omega}^{\parallel} \propto |3\chi_{bcc}^{(2)}\cos^2\theta\sin\theta + \chi_{bbb}^{(2)}\sin^3\theta|^2 \quad (1)$$

$$I_{2\omega}^{\perp} \propto |\chi_{bcc}^{(2)}\cos^3\theta - 2\chi_{bcc}^{(2)}\sin^2\theta\cos\theta + \chi_{bbb}^{(2)}\sin^2\theta\cos\theta|^2 \quad (2)$$

where θ is the polarization angle of the pump beam with respect to the crystallographic c-axis, $\chi_{bbb}^{(2)}$ and $\chi_{bcc}^{(2)}$ are the two independent elements of the second-order nonlinear susceptibility tensor for NbOI₂ crystal. The theoretical fits are also plotted in Figure 3a–c with solid lines showing good agreement with the experimental data. The polarization-resolved THG emission is characterized with the b-component and c-component plotted in Figure 3d,e. The b-component of THG emission has a twofold profile with the maximum THG intensity occurring along the b-axis, while the c-component of THG emission has a butterfly-shaped profile oriented along the c-axis. The c-component of THG emission is relatively stronger than the b-component,
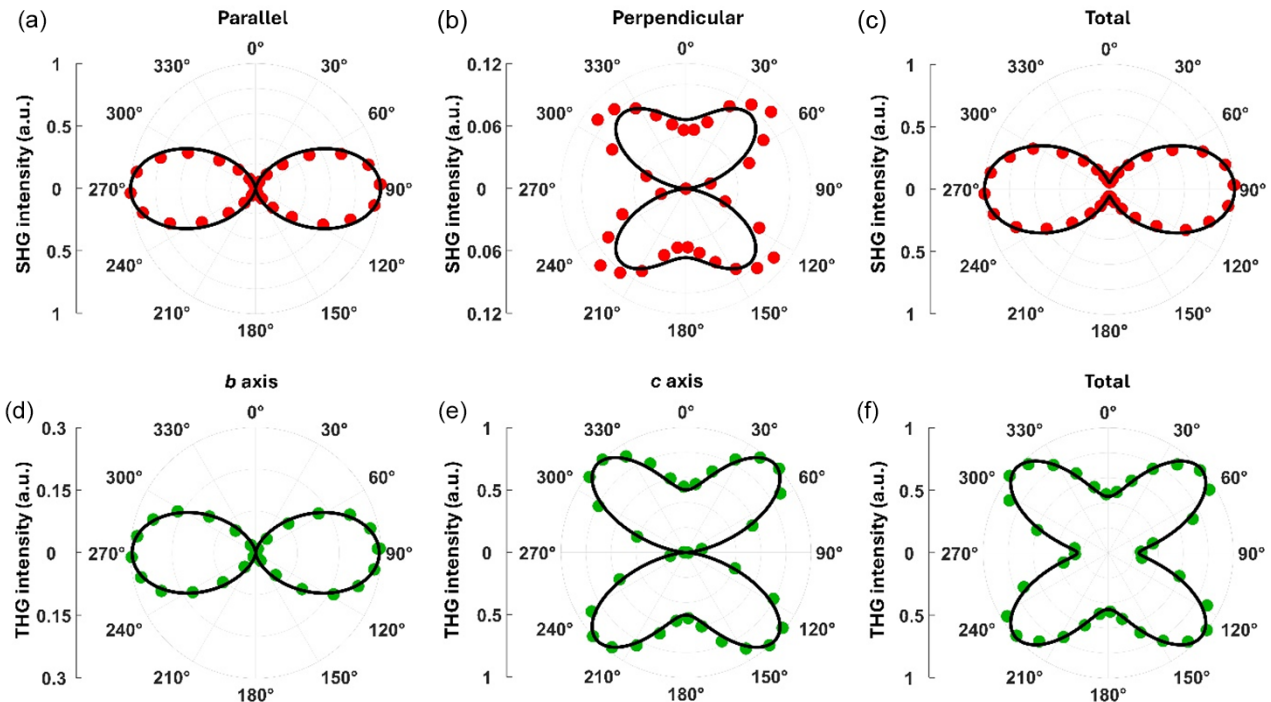

Figure 3. Polarization-resolved nonlinear measurements of the NbOI₂ flake shown in Figure 1. a) Parallel component, b) perpendicular component, and c) total SHG intensity as a function of the pump polarization angle. d) b-component, e) c-component, and f) total THG intensity as a function of the pump polarization angle. Solid lines are the theoretical fits to the experimental data shown as dots. The crystallographic b-axis is oriented along the horizontal direction, and the c-axis is along the vertical direction.

which results in a four-lobe pattern for the total THG intensity as plotted in Figure 3f. The theoretical expression for the b and c-components of THG emission from NbOI$_2$ crystal can be written as,[22]

$$I_{3\omega}^{b} \propto |\chi_{bbbb}^{(3)}\sin^3\theta + 3\chi_{bccb}^{(3)}\sin\theta\cos^2\theta|^2 \tag{3}$$

$$I_{3\omega}^{c} \propto |\chi_{cccc}^{(3)}\cos^3\theta + 3\chi_{ccbb}^{(3)}\cos\theta\sin^2\theta|^2 \tag{4}$$

where $\chi_{bbbb}^{(3)}$, $\chi_{bccb}^{(3)}$, $\chi_{cccc}^{(3)}$, and $\chi_{ccbb}^{(3)}$ are the four independent elements of the third-order nonlinear susceptibility tensor for NbOI$_2$ crystal. Figure 3d–f include the theoretical fits with solid lines, which show good agreement with the measured data. As shown in Figure 3f, the minimum total THG intensity occurs as the pump polarization is along the b-axis, whereas the maximum intensity is achieved as the pump polarization is along a direction approximately at 42° angle to the b-axis. The measured THG anisotropy ratio is 3.83 for the flake. From the results presented above, it is shown that the SHG and THG emission from NbOI$_2$ crystal exhibits highly anisotropic responses, which have great potential for realizing polarization-sensitive nonlinear optical devices. Besides, the polarization-resolved nonlinear measurements can serve as powerful tools for identifying the crystallographic orientation of NbOI$_2$ thin flakes.

The NbOI$_2$ grating holograms are designed to encode the beam profile information of the HG$_{01}$ and HG$_{10}$ modes on the NbOI$_2$ crystal. The binary-amplitude modulation of the second-order or third-order nonlinear susceptibility $\chi^{(n)}$ with $n = 2$ or 3 for producing the HG beams can be described as

$$\chi^{(n)}(x,y) = \chi^{(n)}\left\{\frac{1}{2} + \frac{1}{2}sgn\left[\cos\left\{\frac{2\pi x}{\Lambda} - \phi(x,y)\right\}\right.\right.$$
$$\left.\left. - \cos\{\sin^{-1}A(x,y)\}\right]\right\} \tag{5}$$

where Λ is the grating period, $\phi(x,y)$ and $A(x,y)$ are the phase and amplitude profiles of the beam wavefront in the hologram plane. To generate the nonlinear HG$_{01}$ mode in the first diffraction order, the phase profile can be expressed as

$$\phi(x,y) = \begin{cases} \pi & y \geq 0 \\ 0 & y < 0 \end{cases} \tag{6}$$

while the phase profile for generating the nonlinear HG$_{10}$ mode is

$$\phi(x,y) = \begin{cases} \pi & x \geq 0 \\ 0 & x < 0 \end{cases} \tag{7}$$

and the amplitude profiles for both cases are $A(x,y) = 1$.

The designed binary-amplitude grating holograms to simultaneously generate the second- and third-harmonic HG beams are directly milled into the NbOI$_2$ thin flakes using focused ion beam (FIB). The optical microscope image and the scanning electron microscope (SEM) image of the fabricated grating hologram to generate the HG$_{01}$ mode on a NbOI$_2$ flake with the thickness of 70 nm are shown in **Figure 4**a,b, where the grating lines are oriented along the c-axis of NbOI$_2$ crystal. The second- and third-harmonic images of the grating hologram at the excitation wavelength of 1560 nm are shown in Figure 4c,d. The far-field images

of the hologram in the Fourier plane are shown in Figure 4e,f, which demonstrate the generation of the nonlinear HG$_{01}$ modes at the second- and third-harmonic wavelengths in the first diffraction order. The diffraction angles of the HG$_{01}$ modes can be calculated as $\theta_d = \sin^{-1}(\lambda/\Lambda)$ where λ is the second or third-harmonic wavelength and the grating period $\Lambda = 3$ μm. The diffraction angles are ≈15.1° and 10.0° for the HG$_{01}$ modes at the second- and third-harmonic wavelengths, respectively. Next, the anisotropic response of the second-harmonic HG$_{01}$ mode is characterized by rotating the pump linear polarization and measuring the mode intensity, which is plotted in Figure 4g as red triangles. Highly anisotropic SHG response of the generated HG$_{01}$ mode is observed, which shows a twofold profile with the maximum intensity occurring for the pump polarization along the b-axis and the minimum intensity occurring for the polarization along the c-axis. For comparison, the polarization dependance of the SHG intensity from the bare flake is also plotted in Figure 4g as black squares. The measured anisotropy ratio of the generated second-harmonic HG$_{01}$ mode is 14.95, which is close to the value of 17.36 for the bare flake. The theoretical fits according to Equations (1) and (2) are plotted in Figure 4g as solid lines, indicating good agreement with the measurements. Furthermore, the anisotropic response of the third-harmonic HG$_{01}$ mode is measured and plotted in Figure 4h as green triangles. A four-lobe pattern is observed with the maximum intensity appearing for the pump polarization along a direction approximately at 42° angle to the b-axis and the minimum intensity occurring for the polarization along the b-axis. Figure 4h also plots the polarization dependance of the THG intensity from the bare flake shown as black squares. The measured anisotropy ratio of the third-harmonic HG$_{01}$ mode is 4.85, which is close to the value of 3.73 for the bare flake. The theoretical fits using Equations (3) and (4) are also plotted in Figure 4h as solid lines, showing good agreement with the experimental data.

Next, the measurements are extended to generate anisotropic second- and third-harmonic HG$_{10}$ modes using NbOI$_2$ grating hologram. **Figure 5**a,b display the optical microscope image and the SEM image of the fabricated hologram on a 45 nm-thick NbOI$_2$ flake with the grating lines oriented along the c-axis. The second- and third-harmonic images of the hologram are shown in Figure 5c,d. The corresponding far-field images of the hologram at the second- and third-harmonic wavelengths are shown in Figure 5e,f, demonstrating the generation of nonlinear HG$_{10}$ modes. The polarization dependences of the SHG and THG intensities of the generated HG$_{10}$ modes are plotted in Figure 5g,h as red triangles and green triangles, respectively, showing strong anisotropic responses. The anisotropic responses of the SHG and THG intensities from the bare flake are also included in Figure 5g,h as black squares. The theoretical fits from Equation (1)–(4) are plotted as solid lines, showing good agreement with the measured results. Similar to the case of HG$_{01}$ mode, the second-harmonic HG$_{10}$ mode has a twofold profile with the maximum intensity along the b-axis, while the third-harmonic HG$_{10}$ mode has a four-lobe pattern with the maximum intensity occurring approximately at 39° angle to the b-axis. The measured anisotropy ratios of the second- and third-harmonic HG$_{10}$ modes are 14.92 and 4.33, respectively, which are close to the values of 16.21 and 3.97 for the bare flake.
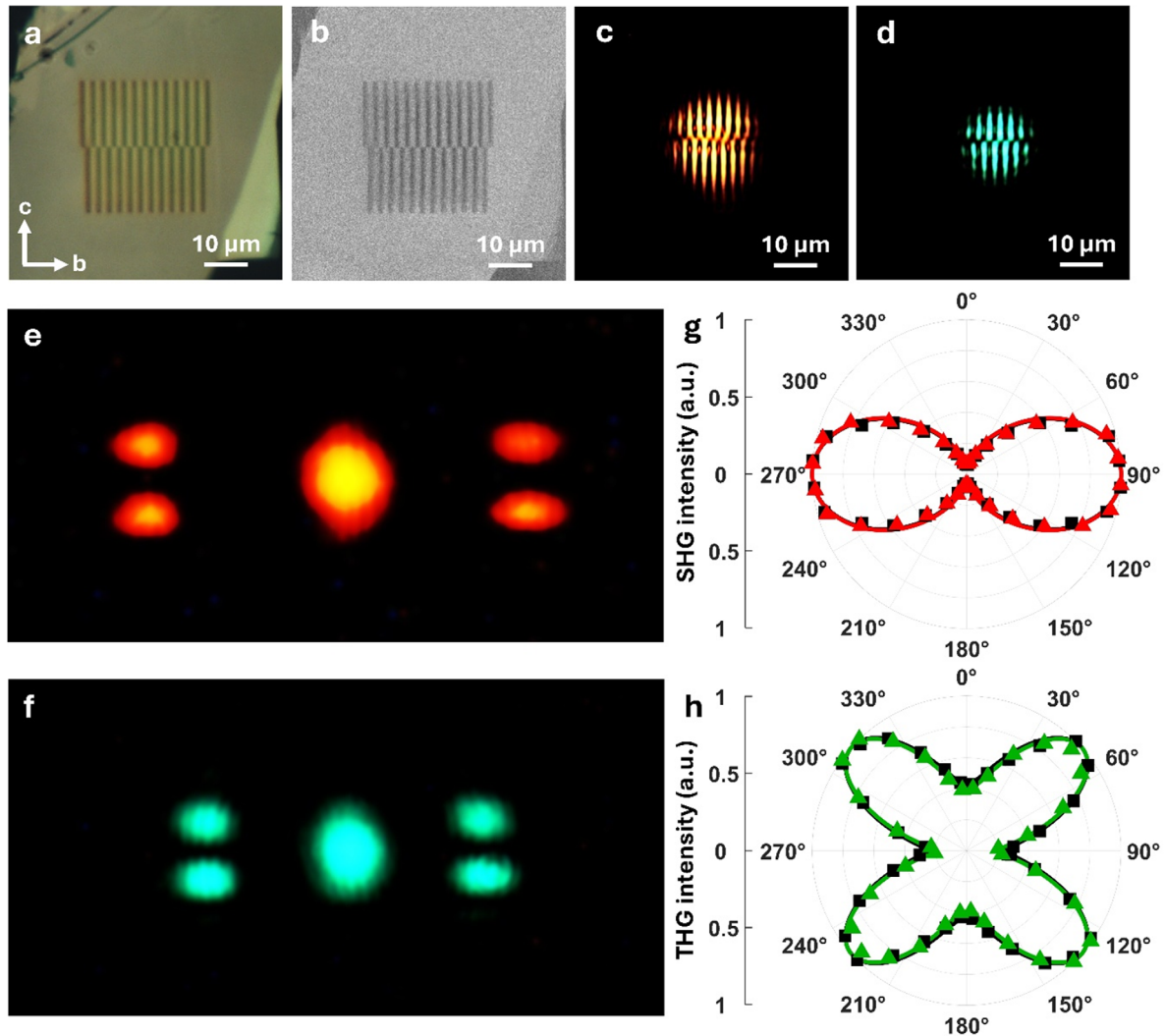
Figure 4. Generation of anisotropic second- and third-harmonic HG_{01} modes. a) Optical microscope image, b) SEM image, c) second-harmonic image, and d) third-harmonic image of the hologram. Far-field images of the hologram with the generated e) second-harmonic and f) third-harmonic HG_{01} modes in the first diffraction order. g) Polarization dependance of the SHG intensity of HG_{01} mode (red triangles) and the SHG intensity from the bare flake (black squares). h) Polarization dependance of the THG intensity of HG_{01} mode (green triangles) and the THG intensity from the bare flake (black squares). Solid lines are theoretical fits to the experimental data.

The nonlinear conversion efficiency of the hologram η_{CE} can be determined as the ratio of the generated SHG or THG power to the pump power. For measuring the SHG conversion efficiency, the pump polarization is set along the b-axis corresponding to the maximum SHG intensity, while for the THG case the pump polarization is along 45° to the b-axis, which is close to the angle for reaching the maximum THG intensity. The average pump power is 72 mW for the SHG measurements, which corresponds to a peak irradiance of 1.75 GW cm^{-2} on the hologram. The SHG conversion efficiencies are 9.72×10^{-10} for the HG_{01} hologram and 1.19×10^{-9} for the HG_{10} hologram. The average pump power for the THG measurements is 210 mW corresponding to a peak irradiance of 5.10 GW cm^{-2}. The THG conversion efficiencies for the HG_{01} and HG_{10} holograms are 1.05×10^{-10} and 2.14×10^{-10}, respectively. The nonlinear HG mode

conversion efficiency is defined as $\eta_{HG} = \eta_{CE}.\eta_{DE}$ where η_{DE} is the diffraction efficiency of the HG mode representing the fraction of SHG or THG power coupled to the first diffraction order. The diffraction efficiencies of the HG_{01} mode and HG_{10} mode for the SHG process are calculated as 43.9% and 48.3%, respectively. The second-harmonic HG mode conversion efficiencies are then determined as 4.27×10^{-10} and 5.77×10^{-10} for the HG_{01} hologram and HG_{10} hologram, respectively. Subsequently, the diffraction efficiencies of the HG_{01} mode and HG_{10} mode for the THG process are 53.3% and 44.7%, respectively. The corresponding third-harmonic HG mode conversion efficiencies are 5.58×10^{-11} and 9.58×10^{-11} for the HG_{01} hologram and HG_{10} hologram, respectively. It is noted that the FIB milling process using gallium ions can introduce undesired nanoscale defects, edge roughness, and amorphous layers
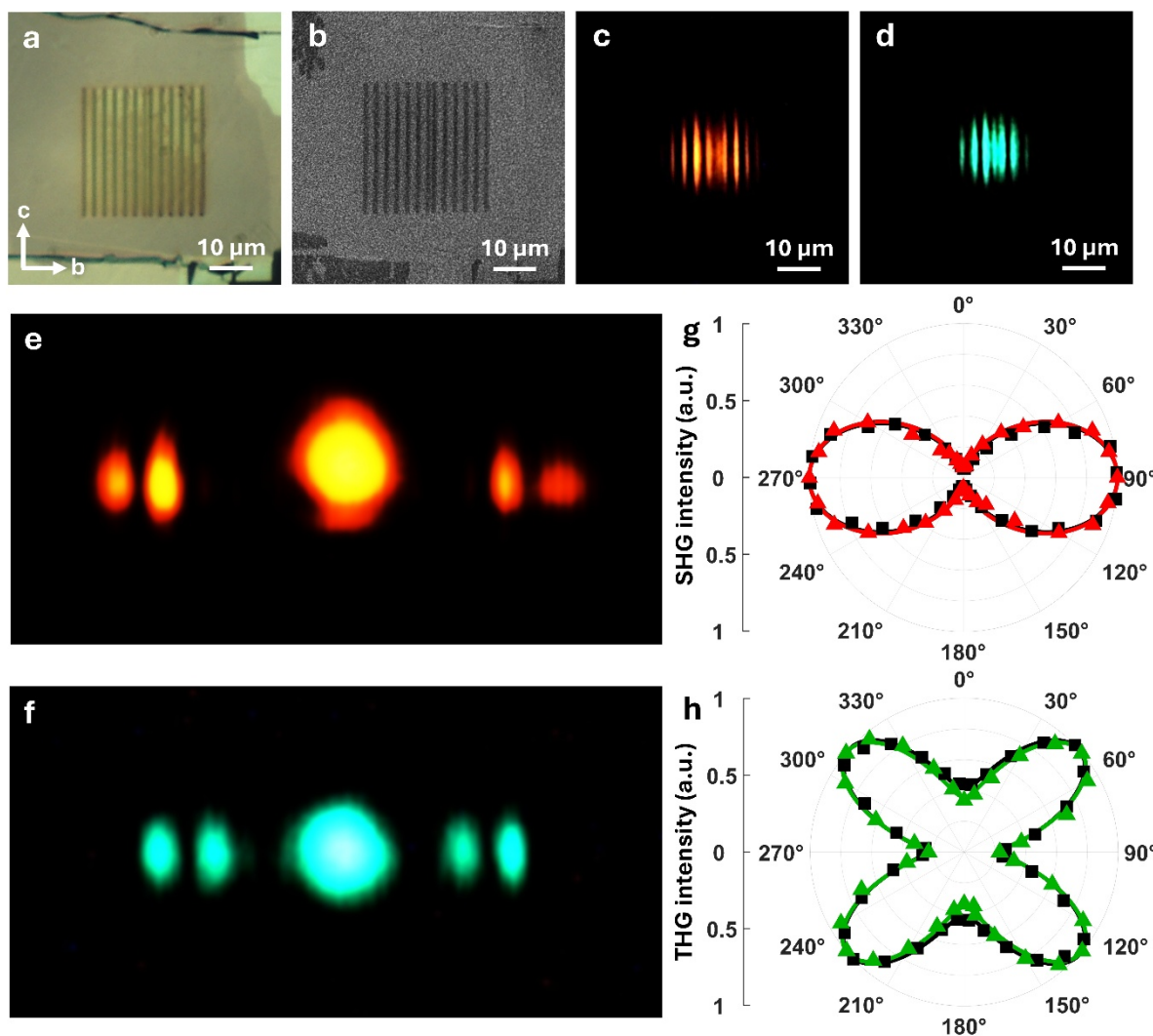
**ADVANCED
SCIENCE NEWS**

www.advancedsciencenews.com

**ADVANCED
PHOTONICS
RESEARCH**

www.adpr-journal.com

Figure 5. Generation of anisotropic second- and third-harmonic HG_{10} modes. a) Optical microscope image, b) SEM image, c) second-harmonic image, and d) third-harmonic image of the hologram. Far-field images of the hologram with the generated e) second-harmonic and f) third-harmonic HG_{10} modes in the first diffraction order. g) Polarization dependance of the SHG intensity of HG_{10} mode (red triangles) and the SHG intensity from the bare flake (black squares). h) Polarization dependance of the THG intensity of HG_{10} mode (green triangles) and the THG intensity from the bare flake (black squares). Solid lines are theoretical fits to the experimental data.

at the grating groove edges of the fabricated holograms. These effects can potentially reduce the diffraction efficiencies of the holograms and the nonlinear HG mode conversion efficiencies.

The relative magnitudes of the second- and third-order nonlinear susceptibility tensor elements of $NbOI_2$ crystal can be retrieved for the bare flakes and the grating holograms according to the theoretical fits from Equations (1)–(4), which are summarized in **Table 1**. The value of the second-order nonlinear susceptibility element $\chi_{bcc}^{(2)}$ are found in the range of 0.23–0.26. The theoretical SHG anisotropy ratio is proportional to the square of the ratio $\chi_{bbb}^{(2)}/\chi_{bcc}^{(2)}$ which is also listed along with the experimental anisotropy ratio. The theoretical SHG anisotropy ratio varies from 14.79 to 18.90 for different samples considered here, which is consistent with the experimentally measured SHG anisotropy ratio varying from 14.92 to 17.73. The theoretical

THG anisotropy ratio is dependent on the relative magnitudes of four different third-order nonlinear susceptibility elements which are listed in Table 1. The extracted relative magnitudes of $\chi_{ccbb}^{(3)}$, $\chi_{bbbb}^{(3)}$, and $\chi_{bccb}^{(3)}$ by setting $\chi_{cccc}^{(3)}$ into unity are in the range of 1–1.16, 0.72–0.80 and 0.18–0.20, respectively. The theoretical THG anisotropy ratio changes from 3.79 to 4.89 for the bare flakes and the holograms, which is very close to the measured THG anisotropy ratio in the range of 3.73 to 4.85. The variations of the SHG and THG anisotropy ratios and correspondingly the nonlinear susceptibility tensor elements between $NbOI_2$ thin flakes can be attributed to the mechanical exfoliation process during the transfer of the crystals to glass substrates, while the variations in the cases of the holograms can be attributed to the defects introduced by gallium ions during the FIB milling process which can alter the crystal structure and electronic properties.[37]

Table 1. Summary of the relative magnitudes of second- and third-order nonlinear susceptibility tensor elements of NbOI$_2$ crystal along with the fitted and experimental SHG and THG anisotropy ratios for the bare flakes and the fabricated holograms.

Sample	SHG			THG				
	$\chi_{bbb}^{(2)}$	$\chi_{bcc}^{(2)}$	Anisotropy (Fit/Exp.)	$\chi_{cccc}^{(3)}$	$\chi_{ccbb}^{(3)}$	$\chi_{bbbb}^{(3)}$	$\chi_{bccb}^{(3)}$	Anisotropy (Fit/Exp.)
Flake 1	1	0.23	18.90/17.73	1	1.00	0.74	0.18	4.05/3.83
Flake 2	1	0.24	17.36/17.36	1	1.02	0.78	0.19	3.79/3.73
HG$_{01}$	1	0.26	14.79/14.95	1	1.10	0.72	0.18	4.89/4.85
Flake 3	1	0.25	16.00/16.21	1	1.05	0.76	0.19	4.14/3.97
HG$_{10}$	1	0.26	14.79/14.92	1	1.16	0.80	0.20	4.37/4.33

3. Conclusion

The generation of highly anisotropic second- and third-harmonic HG beams has been demonstrated with ultrathin NbOI$_2$ grating holograms. The binary-amplitude holograms are designed and fabricated on NbOI$_2$ thin flakes to produce the nonlinear HG$_{01}$ and HG$_{10}$ modes at the second- and third-harmonic wavelengths. It is shown that the generated second-harmonic and third-harmonic HG modes exhibit high anisotropy ratios. The observed strong anisotropic responses in the nonlinear HG modes are due to the in-plane anisotropic lattice structure of NbOI$_2$ crystal. The relative magnitudes of the nonlinear susceptibility tensor elements of NbOI$_2$ crystal are further retrieved through the theoretical fits of the polarization-dependent SHG and THG intensities. The simultaneous generation of second- and third-harmonic Hermite–Gaussian modes as well as the demonstrated strong anisotropic responses in ultrathin nonlinear photonic devices will pave the way for advancing future applications in photonic integrated circuits, quantum photonic chips, optical computing, and optical communication. For example, Hermite–Gaussian modes have been utilized for the generation of squeezed states with a high quantum noise reduction, as well as the quantum interference of entangled photon pairs.[13,38] Furthermore, Hermite–Gaussian beams offer great potential to significantly enhance data capacity in optical communication and optical computing through spatial mode-division multiplexing due to the orthogonality of the modes,[6–8,39,40] along with the reduced mode cross-talk and mode-dependent loss.[41]

4. Experimental Section

Sample Preparation: NbOI$_2$ thin flakes were first exfoliated to polydimethylsiloxane (PDMS) layers using scotch tape from bulk crystals (HQ graphene) and then transferred to glass substrates. Before the transfer, the glass substrates were cleaned using acetone and isopropyl alcohol. Next, the sample was spin coated with a water-soluble conductive polymer layer to avoid surface charge accumulation. The holograms were fabricated using FIB milling with gallium ions to form the patterned area of $30 \times 30\ \mu m^2$. The conductive polymer layer was removed after patterning using deionized water and finally the sample was blown dry using nitrogen gas.

Optical Setup: The linearly polarized pump beam at 1560 nm (Calmer fiber laser, pulse width 90 fs, repetition rate 80 MHz) was focused on the sample by using a $4\times$ objective lens with numerical aperture (NA) of 0.12. The laser spot diameter on the sample was around 27 μm, which illuminates the hologram area. The transmitted signal was collected using a $20\times$ objective lens with NA of 0.42. The signal was then passed through a 900 nm shortpass filter to reject the pump beam, and a 780 or 520 nm bandpass filter to select the SHG or THG emission. Finally, the nonlinear signal was imaged either in Fourier space or real space with a color charge-coupled device camera. The SHG and THG spectra were obtained using an optical spectrometer (Horiba, iHR550).

Conflict of Interest

The authors declare no conflict of interest.

Data Availability Statement

The data that support the findings of this study are available from the corresponding author upon reasonable request.

[1] B. E. A. Saleh, M. C. Teich, *Fundamentals of Photonics*, Wiley, New Jersey **2019**, Ch. 3.

[2] D. Weber, R. Heimburger, D. Hildebrand, T. Junghans, G. Schondelmaier, C. Walther, D. Schondelmaier, *Appl. Phys. A* **2019**, *125*, 307.

[3] S. Pirandola, B. R. Bardhan, T. Gehring, C. Weedbrook, S. Lloyd, *Nat. Photonics* **2018**, *12*, 724.

[4] A. P. Porfirev, R. V. Skidanov, *J. Opt. Technol.* **2015**, *82*, 587.

[5] M. Woerdemann, C. Alpmann, M. Esseling, C. Denz, *Laser Photonics Rev.* **2013**, *7*, 839.

[6] M. A. Cox, L. Maqondo, R. Kara, G. Milione, L. Cheng, A. Forbes, *J. Lightwave Technol.* **2019**, *37*, 3911.

**ADVANCED
SCIENCE NEWS**

www.advancedsciencenews.com

**ADVANCED
PHOTONICS
RESEARCH**

www.adpr-journal.com

[7] K. Pang, H. Song, Z. Zhao, R. Zhang, H. Song, G. Xie, L. Li, C. Liu, J. Du, A. F. Molisch, M. Tur, A. E. Willner, *Opt. Lett.* **2018**, *43*, 3889.

[8] M. Balogun, S. Derevyanko, *J. Lightwave Technol.* **2022**, *40*, 6071.

[9] S. Ast, S. D. Pace, J. Millo, M. Pichot, M. Turconi, N. Christensen, W. Chaibi, *Phys. Rev. D* **2021**, *103*, 042008.

[10] I. Dolev, I. Epstein, A. Arie, *Phys. Rev. Lett.* **2012**, *109*, 203903.

[11] N. Yu, F. Capasso, *Nat. Mater.* **2014**, *13*, 139.

[12] S. Keren-Zur, O. Avayu, L. Michaeli, T. Ellenbogen, *ACS Photonics* **2016**, *3*, 117.

[13] J. Heinze, B. Willke, H. Vahlbruch, *Phys. Rev. Lett.* **2022**, *128*, 083606.

[14] Q. Ma, G. Ren, K. Xu, J. Z. Ou, *Adv. Optical Mater.* **2021**, *9*, 2001313.

[15] A. Autere, H. Jussila, Y. Dai, Y. Wang, H. Lipsanen, Z. Sun, *Adv. Mater.* **2018**, *30*, 1705963.

[16] J. W. You, S. R. Bongu, Q. Bao, N. C. Panoiu, *Nanophotonics* **2019**, *8*, 63.

[17] Z. Xie, T. Zhao, X. Yu, J. Wang, *Small* **2024**, *20*, 2311621.

[18] C. Trovatello, A. Marini, M. Cotrufo, A. Alù, P. J. Schuck, G. Cerullo, *ACS Photonics* **2024**, *11*, 2860.

[19] A. Dasgupta, J. Gao, X. Yang, *Laser Photonics Rev.* **2020**, *14*, 1900416.

[20] H. Sar, J. Gao, X. Yang, *Sci. Rep.* **2021**, *11*, 6372.

[21] R. P. N. Tripathi, X. Yang, J. Gao, *Opt. Express* **2022**, *30*, 22661.

[22] H. Sar, J. Gao, X. Yang, *Sci. Rep.* **2020**, *10*, 14282.

[23] X. Li, H. Liu, C. Ke, W. Tang, M. Liu, F. Huang, Y. Wu, Z. Wu, J. Kang, *Laser Photonics Rev.* **2021**, *15*, 2100322.

[24] J. Wang, C. Z. Jiang, W. Q. Li, X. H. Xiao, *Adv. Optical Mater.* **2022**, *10*, 2102436.

[25] S. H. Suk, S. B. Seo, Y. S. Cho, J. Wang, S. Sim, *Nanophotonics* **2024**, *13*, 107.

[26] C. Tan, P. Yu, Y. Hu, J. Chen, Y. Huang, Y. Cai, Z. Luo, B. Li, Q. Lu, L. Wang, Z. Liu, H. Zhang, *J. Am. Chem. Soc.* **2015**, *137*, 10430.

[27] D. Li, H. Jussila, L. Karvonen, G. Ye, H. Lipsanen, X. Chen, Z. Sun, *Sci. Rep.* **2015**, *5*, 15899.

[28] Y. Ma, H. Yi, H. Liang, W. Wang, Z. Zheng, J. Yao, G. Yang, *Mater. Futures* **2024**, *3*, 012301.

[29] H. Liu, C. Zhu, Y. Chen, X. Yi, X. Sun, Y. Liu, H. Wang, G. Wu, J. Wu, Y. Li, X. Zhu, D. Li, A. Pan, *Adv. Funct. Mater.* **2024**, *34*, 2314838.

[30] Y. Jia, Y. Zhao, G. Gou, X. C. Zeng, J. Li, *Nanoscale Horiz.* **2019**, *4*, 1113.

[31] L. Ye, W. Zhou, D. Huang, X. Jiang, Q. Guo, X. Cao, S. Yan, X. Wang, D. Jia, D. Jiang, Y. Wang, X. Wu, X. Zhang, Y. Li, H. Lei, H. Gou, B. Huang, *Nat. Commun.* **2023**, *14*, 5911.

[32] T. Fu, K. Bu, X. Sun, D. Wang, X. Feng, S. Guo, Z. Sun, Y. Fang, Q. Hu, Y. Ding, T. Zhai, F. Huang, X. Lü, *J. Am. Chem. Soc.* **2023**, *145*, 16828.

[33] I. Abdelwahab, B. Tilmann, Y. Wu, D. Giovanni, I. Verzhbitskiy, M. Zhu, R. Berté, F. Xuan, L. d. S. Menezes, G. Eda, T. C. Sum, S. Y. Quek, S. A. Maier, K. P. Loh, *Nat. Photon.* **2022**, *16*, 644.

[34] W. Chen, S. Zhu, S. Duan, C. Wang, F. Wang, Y. Wu, M. Dai, J. Cui, S. H. Chae, Z. Li, X. Ma, Q. Wang, Z. Liu, Q. J. Wang, *Adv. Mater.* **2024**, *36*, 2400858.

[35] Q. Guo, Y. Wu, D. Zhang, Q. Zhang, G. Guo, A. Alù, X. Ren, C. Qiu, *Nat. Commun.* **2024**, *15*, 10461.

[36] Q. Guo, X. Qi, L. Zhang, M. Gao, S. Hu, W. Zhou, W. Zang, X. Zhao, J. Wang, B. Yan, M. Xu, Y. Wu, G. Eda, Z. Xiao, S. A. Yang, H. Gou, Y. P. Feng, G. Guo, W. Zhou, X. Ren, C. Qiu, S. J. Pennycook, A. T. S. Wee, *Nature* **2023**, *613*, 53.

[37] J. Deka, J. Gao, X. Yang, *Laser Photonics Rev.* **2025**, *19*, 2401519.

[38] Y. Zhang, S. Prabhakar, C. Rosales-Guzmán, F. S. Roux, E. Karimi, A. Forbes, *Phys. Rev. A* **2016**, *94*, 033855.

[39] M. Singh, J. Malhotra, *J. Opt. Commun.* **2023**, *44*, 495.

[40] X. Yu, J. Meier, P. Mandal, M. I. Hosni, A. Venugopalan, L. Wang, T. Schneider, *Sci. Rep.* **2025**, *15*, 486.

[41] B. Ndagano, N. Mphuthi, G. Milione, A. Forbes, *Opt. Lett.* **2017**, *42*, 4175.